Effects of tropical cyclones on large-scale circulation and ocean heat transport in the South China Sea

Xidong Wang · Chunzai Wang · Guijun Han ·
Wei Li · Xinrong Wu

Abstract In this study, we investigate the influence of tropical cyclones (TCs) on large-scale circulation and ocean heat transport in the South China Sea (SCS) by using an ocean general circulation model at a 1/8° resolution during 2000–2008. The model uses a data assimilation system to assimilate observations in order to improve the representation of SCS circulation. The results reveal an unexpected deep SCS circulation anomaly induced by TCs, which suggests that effects of TC can penetrate deeper into the ocean. This deep effect may result from the near inertial oscillations excited by TCs. The inertial oscillations can propagate downward to the oceanic interior. The analyses confirm that TCs have two effects on ocean heat transport of the SCS. Firstly, the wind stress curl induced by TCs affects the structure of SCS circulation, and then changes heat transport. Secondly, TCs pump surface heat downward to the thermocline, increasing the heat injection from the atmosphere to the ocean. Two effects together amplify the outflow of the surface heat southward away the SCS through the Mindoro and Karimata Straits. The TC-induced heat transports through the Mindoro, Balabac and Karimata Straits account for 20 % of the total heat transport through three straits. An implication of this study is that ocean models need to simulate the TC effect on heat transport in order to correctly evaluate the role of the SCS through flow in regulating upper ocean circulation and climate in the Indonesian maritime continent and its adjacent regions.

Keywords South China Sea circulation · Tropical cyclone · Heat transport · Air-sea interaction

X. Wang
Cooperative Institute for Marine and Atmospheric Studies,
University of Miami, Miami, FL, USA

X. Wang · C. Wang
NOAA/Atlantic Oceanographic and Meteorological Laboratory,
Miami, FL, USA

X. Wang (✉) · G. Han · W. Li · X. Wu
Key Laboratory of Marine Environmental Information
Technology, SOA, National Marine Data and Information
Service, 93 Liuwei Road, Hedong District, Tianjin 300171,
China
e-mail: xidong_wang@yahoo.com

1 Introduction

The South China Sea (SCS) is the largest semi-enclosed marginal sea in the northwest Pacific with several passages linking to neighboring waters. The SCS is surrounded by the Asian continent to the north and west, the Philippine Islands to the east, Borneo Island to the southeast and Indonesia to the south. It connects with the East China Sea, the Pacific Ocean, the Sulu Sea, the Java Sea and the Indian Ocean through the Taiwan Strait, the Luzon Strait, the Mindoro Strait, the Balabac Strait, the Karimata Strait and the Malacca Strait, respectively. Situated at the pathway of the East Asian monsoon system, SCS circulation is largely influenced by the seasonal reversal of monsoonal winds, northeasterly in winter and southwesterly in summer. The SCS upper-layer circulation is primarily driven by the SCS monsoon wind (Wyrtki 1961). On seasonal timescale, there is a basin-wide cyclonic gyre in winter, while the circulation separates into a weak cyclonic gyre north of about 12°N and a strong anticyclonic gyre south of 12°N in summer. Beyond seasonal timescale, the SCS circulation shows an interannual variation related to El Niño/Southern Oscillation (ENSO) (e.g., Wu et al. 1998; Wang et al. 2006a).

Another important characteristic of the SCS circulation is to have an average current through the SCS, namely, the

SCS throughflow (SCSTF) which is constituted by the inflow from the Kuroshio through the Luzon Strait and outflow through the Mindoro, Karimata, and Taiwan Straits (e.g., Qu 2000; Qu et al. 2005, 2006a; Wang et al. 2006b). Previous studies have shown that the intrusion of freshwater from the SCS effectively inhibited the Makassar Strait surface water from freely flowing southward and as a consequence, the Indonesian throughflow (ITF) heat transport was significantly reduced during the northeast monsoon season (Gordon et al. 2003). Qu et al. (2005, 2006a) suggested that the SCSTF is a heat conveyor, transferring heat from the SCS into the Indonesian Seas and thus has a notable impact on heat transport of the ITF. Gordon (2005) hypothesized that the outflow from the Karimata and Mindoro Straits was important for determining the thermohaline structure of the ITF. Thus, the SCSTF can impact large-scale circulation and climate in the Indian and Pacific Oceans.

Tropical cyclone (TC) or typhoon is one of the most destructive nature phenomena. The mixing and upwelling induced by TC winds can vigorously reduce sea surface temperature (SST) beneath a moving TC, leaving behind a cold SST wake. This cold wake can exist in the ocean for days to weeks and generate continual effects on the atmosphere and ocean, even climate variability and climate change. The cold wake has a large influence on the seasonal cycle of SST. TCs occurring in the first half of the season disrupt the seasonal warming trend, which is not resumed until 30 days after TC passage. Conversely, TC occurrences in the second half of the season bring about a mean temperature drop of approximately 0.5 °C, from which the ocean does not recover due to the seasonal cooling cycle (Dare and Mcbride 2011). It was found that the persistence of SST anomalies for 1–2 months after the TC passage could potentially affect large-scale atmospheric circulation (Hart et al. 2007). Several studies, based on observations and models, suggested that TC-induced energy input and mixing may play an important role in climate variability, regulating the oceanic general circulation and its variability (e.g., Emanuel 2001, 2005; Kossin et al. 2007; Liu et al. 2008; Hu and Meehl 2009; Fedorov et al. 2010).

TCs can cause downward pumping of huge amount of surface heat into the subsurface ocean along their passage and such heat was eventually transported away by ocean currents, and most likely transfers poleward (e.g., Emanuel 2001; Sriver and Huber 2007; Pasquero and Emanuel 2008). In fact, it is an unresolved issue where ocean heat uptake (OHU) pumped by TCs will eventually go. Some idealized modeling studies in which the effect of TCs was represented as an increased diffusivity (Korty et al. 2008; Jansen and Ferrari 2009; Sriver et al. 2010) have attempted to quantify TC influence on ocean heat transport. Their

results indicated that magnitude of the poleward heat transport associated with TCs was sensitive to TC-induced mixing extent in longitude and latitude. Besides, several studies argued that TC-induced OHU has been overestimated in the observation-based studies (Emanuel 2001; Sriver and Huber 2007; Sriver et al. 2008) because most of them assumed that all heat pumped downward to the mixed layer base during the TC season completely remained in the ocean (Jansen et al. 2010; Vincent et al. 2012). Due to neglecting seasonal variability of the mixed layer depth, three quarter of OHU induced by TCs was overestimated (Jansen et al. 2010). If considering heat extraction by TC winds during their passages, zonal compensations and equatorward transport, only one-tenth of the OHU was actually exported poleward (Vincent et al. 2012).

The above-mentioned studies mainly focus on the issue of what role TCs play in the global or regional open ocean climate system and of how TCs affect the long-term meridional heat transport in global scale. The SCS is one of the most active regions where TCs occur frequently. TCs over the SCS impacted by the Asian monsoon system have seasonal variation, which has been discussed in previous studies (e.g., Wang et al. 2007). However, little investigation is given for influence of TCs on large-scale circulation and heat transport of the SCS, except that Wang et al. (2009) discussed the effect of TCs on seasonal circulation of the SCS using a simple 1.5 layer reduced-gravity ocean model. Because the SCS circulation has the potential to affect circulation and climate in the Indian and Pacific Oceans, the present paper investigates the contribution of TCs to large-scale circulation and heat transport of the SCS. In this study, an oceanic general circulation model (GCM) with the data assimilation system is used to improve the representation of the SCS circulation without the passage of TCs.

The rest of the paper is organized as follows. Section 2 depicts the ocean model and data assimilation scheme. Section 3 investigates oceanic annual-mean response to TCs. Section 4 describes seasonal cycle of oceanic thermal response. Section 5 evaluates the TC influence on ocean heat transport. Section 6 summarizes the main conclusions.

2 Methodology and data

2.1 Numerical model and data assimilation scheme

The Princeton Ocean Model with generalized coordinate system (POMgcs) is used. The model region is from 10°S to 52°N and 99°E to 150°E. The model grid varies from 1/2° to 1/8°. The ocean model has a 1/8° resolution in the SCS and its adjacent oceans. Due to the complicated bathymetry of the study area, the hybrid coordinate of

POMgcs is used following the study of Mellor et al. (2002). Simple Ocean Data Assimilation (SODA) monthly-mean product of the calendar year is used to serve as the open boundary conditions for sea surface height (SSH), temperature, salinity and velocity in the ocean model. The ocean model is forced by the National Centers for Environmental Prediction (NCEP) reanalysis heat flux and surface wind from a new Cross-Calibrated, Multi-Platform (CCMP) ocean surface wind product with the spatial resolution of 0.25° × 0.25° and the temporal resolution of 6 h, which is produced by combining all ocean surface wind speed observations from SSM/I, AMSRE and TMI, and all ocean surface wind vector observations from QuikSCAT and SeaWinds. Following Oey et al. (2006), the wind stress is calculated using the bulk formula:

similar variational scheme proposed by Zhu and Yan (2006) is used to convert altimeter SSH anomaly into temperature and salinity "pseudo observations". The basic idea proposed by Troccoli et al. (2002) is employed to make salinity adjustment during temperature assimilation. The data assimilation system used in this study has been given a complete discussion by Han et al. (2011).

To examine the effect of TCs on large-scale circulation and ocean heat transport in the SCS, we adopt the method used by Wang et al. (2009) to reconstruct two sets of wind forcing: one is the original dataset including all TCs and the other is to exclude all TCs in the SCS. A simple temporal linear interpolation is used to reconstruct the wind forcing for those periods during which we exclude TCs. Two experiments are designed: one is forced by the ori-

$$
\tau = \begin{cases} 0.0012\rho_a \times \mathbf{U}_{10}|\mathbf{U}_{10}|, & \text{if } |\mathbf{U}_{10}| \leq 11 \text{ m/s} \\ \rho_a(0.00049 + 0.000065|\mathbf{U}_{10}|) \times \mathbf{U}_{10}|\mathbf{U}_{10}|, & \text{if } 11 < |\mathbf{U}_{10}| \leq 19 \text{ m/s} \\ \rho_a\left(0.001364 + 2.34 \times 10^{-5}|\mathbf{U}_{10}| - 2.3 \times 10^{-7}|\mathbf{U}_{10}|^2\right) \times \mathbf{U}_{10}|\mathbf{U}_{10}|, & \text{if } 19 < |\mathbf{U}_{10}| < 100 \text{ m/s} \end{cases} \tag{1}
$$

where ρ_a is density of air and $\mathbf{U}_{10}$ is wind speed at 10 m. This formula modifies the one by Large and Pond (1981) to incorporate the limited drag coefficient for high wind speeds (Powell et al. 2003).

A sequential three-dimensional variational (3D-Var) analysis scheme is designed to assimilate temperature and salinity based on a multi-grid framework in this study. The multi-grid 3D-Var analysis scheme can be performed in three dimensional space to retrieve resolvable information from longer to shorter wavelengths for a given observation network, which can yield multi-scale analysis. The multi-grid 3D-Var scheme was discussed in detail by Li et al. (2008, 2010) and has been widely used in oceanic and atmospheric data assimilation. In multi-grid 3D-Var analysis, one minimizes the cost function over a coarse grid to obtain long-wave information and the cost function over a relatively fine grid for short-wave information. As the grid is refined from the coarse to the fine, the new observations increment relative to the background are subject to 3D-Var in turn. During the analysis on each grid level, the analysis field obtained on the previous coarser grid level is regarded as background for the next finer grid level and the increment is also relative to the background of the previous coarser grid level. The final result is obtained by summing the analysis from all the grid levels. The specifics of the technique were described in Li et al. (2008, 2010). A

ginal wind including all TCs (hereafter referred to TCF); the other is forced by eliminating TCs wind (hereafter referred to NONTCF). The net heat flux at the sea surface is given as the sum of the radiative, sensible and latent heat components:

$$
Q = Q_r - Q_{SH} - Q_{LH}, \tag{2}
$$

where Q is the net heat flux to the ocean, Q_r is the net radiative gain received by the ocean, Q_{SH} is the sensible heat flux and finally Q_{LH} is the latent heat flux. Q_r is from NCEP with the spatial resolution of 1.875° × 1.875° and 6-h interval. The turbulent heat fluxes, i.e., the sensible and latent heat fluxes, are computed by the bulk formulation using the air temperature, wind speed and specific humidity from NCEP with the spatial resolution of 1.875° × 1.875° and 6-h interval. The bulk expressions of the sensitive and latent heat fluxes are (Fairall et al. 2003)

$$
Q_{SH} = \rho_a C_{pa} C_h U_{10}(T_s - T_a) \tag{3}
$$

$$
Q_{LH} = \rho_a L_e C_e U_{10}(q_s - q_a) \tag{4}
$$

where ρ_a is the density of air, C_h and C_e are the turbulent exchange coefficient for the sensitive and latent flux, C_{pa} is the specific heat capacity of the air at the constant pressure. U_{10} is the wind speed at the 10 m, and L_e [$L_e = (2.501 - 0.00237 \times SST) \times 10^6$] is the latent heat of vaporization.

T_s and T_a are SST and air temperature at the 10 m, respectively. q_s and q_a are the specific humidity at the sea surface and 10 m. In the two experiments, the net radiative heat flux is the same from NCEP, while the turbulent heat flux from the bulk formulae is calculated using the ocean model's SST. Therefore, the negative feedback of SST on the turbulent heat flux can be permitted. The freshwater flux (FW) due to evaporation E and precipitation P are given by $FW = E - P$. Precipitation is provided by NCEP with the spatial resolution of $1.875° \times 1.875°$ and 6-h interval, while evaporation is calculated from the latent heat flux using $E = {Q_{LH}}/{\rho_w L_e}$, where ρ_w is the density of sea water (Fairall et al. 2003). In addition, all observations are not assimilated into the numerical model during the TCs passage and 10 days after TCs passage in both experiments in order to avoid the effect of the observational signal. The model is initialized with the World Ocean Atlas (WOA 05) and forced by the climatological month winds from the International Comprehensive Ocean–Atmosphere Data Set Project (ICOADS) to integrate forward for 50 years in order to make model reach an equilibrium state. Next, the model is run over the period of 2000–2008.

This numerical system has been validated using independent observations in previous study. The results show that this system can better simulate temperature, salinity structure, meso-scale and large-scale circulation in the northwestern Pacific including the SCS (Han et al. 2011). Climatology and season variability of the SCS temperature have been better documented by several earlier studies (e.g., Chu et al. 1997; Qu 2001; Wang and Wang 2006). For the sake of brevity, we don't give a detailed description about temperature climatology and season variability in the present study. They are only given as a benchmark of the TC-induced temperature anomaly.

2.2 Observations

The observational data used in this study include temperature/salinity profiles from the World Ocean Database 2009 (WOD09), the Global Temperature and Salinity Profile Project (GTSPP) and the Array for Real-time Geostrophic Oceanography (Argo), and SSH anomaly from altimeter and SST from satellite remote sensing. These data are assimilated into the numerical model in order to improve the representation of ocean circulation and hydrographic structure of the SCS. The temperature and salinity profiles are subject to complete quality control, including position/time check, depth duplication check, depth inversion check, temperature and salinity range check, excessive gradient check, and stratification stability check, etc. The multi-
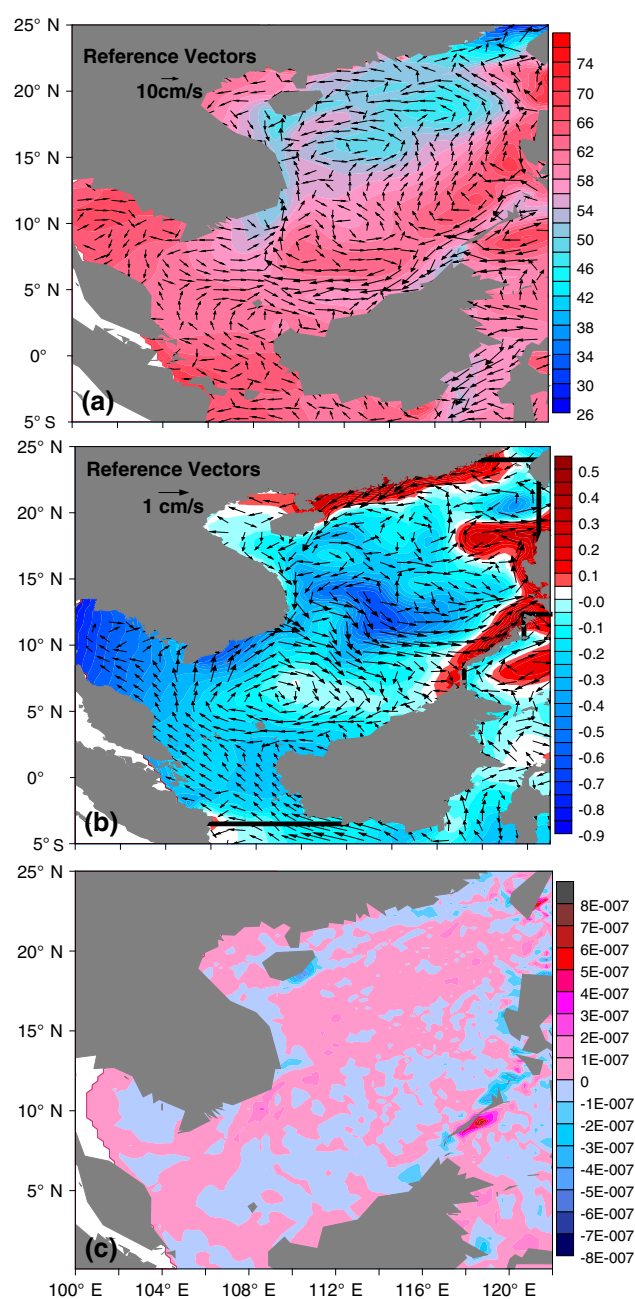

Fig. 1 **a** Horizontal distribution of annual-mean SSH (*shaded*, Unit: cm), averaged velocity of the top 50 m (*vectors*, Unit: cm/s) in the NONTCF experiment. **b** Horizontal distribution of annual-mean SSH difference (*shaded*, Unit: cm), the difference of averaged velocity of the top 50 m (*vectors*, Unit: cm/s) between the TCF and NONTCF experiments. *Solid lines* indicate transects used for the calculation of heat transports through the Taiwan, Luzon, Mindoro, Balabac and Karimata Straits. **c** The difference of averaged divergence of the top 50 m (Unit: s^{-1}) between the TCF and NONTCF experiments

satellite altimeter SSH anomaly is distributed by the Archiving, Validation and Interpretation of Satellite Oceanographic data (AVISO). It consists of maps at 7-day intervals and 1/4° spatial resolution. The product is
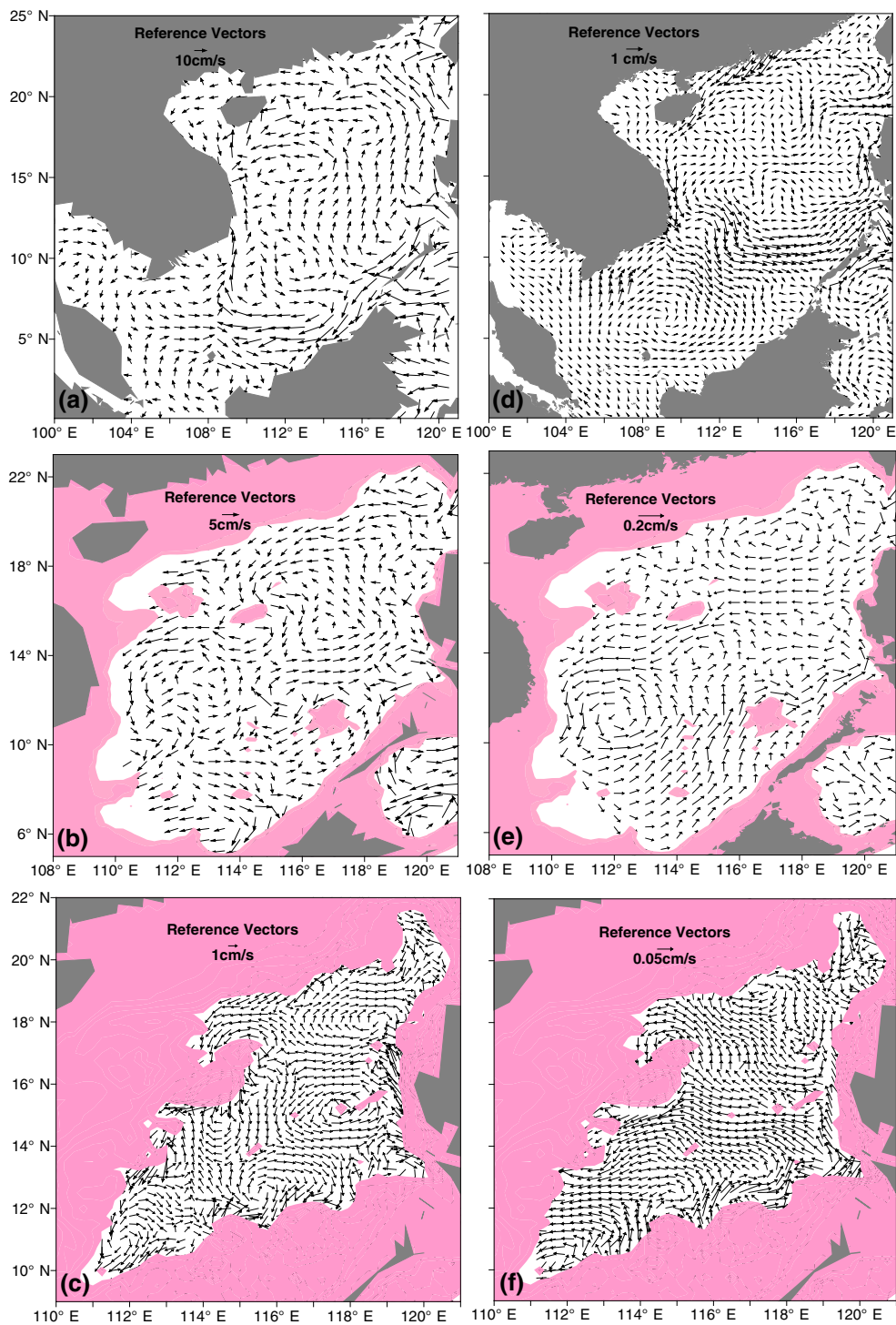
Fig. 2 *Left panels* horizontal distribution of annual-mean current in the NONTCF experiment at **a** 0 m, **b** 1,000 m, **c** 3,000 m; *Right panels* the annual-mean current difference between the TCF and NONTCF experiments at **d** 0 m, **e** 1,000 m, **f** 3,000 m (Unit: cm/s). The *purple shades* indicate water shallower than 1,000 and 3,000 m

developed by merging SSH anomaly data of TOPEX/ Poseidon, JASON-1, GFO, ERS-1/2 and Envisat using optimal interpolation with realistic correlation function (Ducet et al. 2000). The satellite SST is from Reynolds SST data (Reynolds et al. 2007). The spatial resolution is 0.25° × 0.25° and the temporal resolution is daily.

3 Response of annual-mean state to TCs

In this section, we will discuss oceanic response to TCs on the annual-mean state from 2000 to 2008, including sea surface height, ocean circulation and temperature.

3.1 Sea surface height

Figure 1 shows spatial distribution of the NONTCF SSH, and SSH difference, divergence difference between the TCF and NONTCF experiments. A large cyclonic gyre basically exists north of the basin (Fig. 1a), consistent with the result of dynamic height analysis using hydrographic data (Qu 2000). SCS TCs are mostly confined in the north of 12°N, which provide more positive wind stress curl in the northern SCS (Wang et al. 2009). Therefore, Ekman upwelling associated with positive wind stress curl induced by TCs creates a net divergence (Fig. 1c) in the northern SCS basin, which results in a negative SSH anomaly (Fig. 1b). However, within a half-closed ocean basin, in order to balance ocean water mass, the ocean water converges along the western coast of the Luzon Island and the southern coast of China (Fig. 1c), which causes positive SSH anomalies (Fig. 1b). The weak SSH anomalies appear in the 10°N south where there is less TC occurrence (Fig. 1b). These results support that the TC-winds strengthen wind stress curl and contribute to climatological background Ekman pumping (Jullien et al. 2012; Scoccimarro et al. 2011).

3.2 Ocean circulation

Figure 2 displays annual-mean currents in the NONTCF experiment, and the difference between the TCF and NONTCF experiments at the surface (0 m), intermediate (1,000 m), and deep layer (3,000 m). The annual-mean surface circulation (Fig. 2a) is similar to Fig. 1a, which is in better agreement with previous studies (e.g., Qu 2000). The annual-mean intermediate circulation mainly contains two cyclonic gyres that roughly split at the 114°E line (Fig. 2b). Driven by a persistent baroclinic pressure gradient, the colder and higher density Pacific water sinks to the SCS after it crosses the Luzon Strait (Qu et al. 2006b; Li and Qu 2006). It is speculated from temperature, oxygen, and sediment distributions that after entering the SCS, the Pacific overflow water turns northwestward to form a basin-scale cyclonic circulation in the deep SCS (Qu et al. 2006b). The annual-mean deep circulation (Fig. 2c) shows a cyclonic gyre around the seamount at the center of the SCS basin, which is in agreement with previous studies (Qu et al. 2006b; Wang et al. 2011). However, several sub-basin gyres surround the cyclonic gyre (Fig. 2c), which was not presented by geostrophic analysis using thermal wind equation (Wang et al. 2011). In fact, the SCS bottom was driven by the strong mixing from tide and Luzon Strait overflow (Tian and Qu 2012). This indicates that the geostrophic current can only represent part of the deep circulation structure.

Next, we examine how TCs affect the SCS ocean circulation. At the surface layer, TCs induce a cyclonic gyre embedded by anomalous eddy in the north of 12°N, and cause a relatively weak anticyclone gyre in the south of 12°N. The cyclone and anticyclone gyres enhance southward and northward currents along the western boundary of the SCS, respectively. There is a strong eastward jet along about 12°N where the north cyclonic and south anticyclonic gyres are separated (Fig. 2d). TC-induced current pattern in the surface is remarkably similar to the summer SCS circulation structure in the upper ocean. Due to the Asian monsoon influence, TCs over the SCS have a strong seasonal variation. The busy months of SCS TCs appear from July to September (Wang et al. 2007), which can induce a positive (negative) wind stress curl in the northwestern (southeastern) SCS in summer (Wang et al. 2009). These suggest that TCs can boost the formation of summer SCS circulation structure, which is consistent with Wang et al. (2009). At the 1,000 m level, TCs induce a double gyre pattern with an anticyclonic gyre in the north of 15°N, and with a cyclonic gyre in the south of 15°N (Fig. 2e). In the 3,000 m level, due to the topography effect, TCs induce two irregular gyres including an anticyclonic gyre in the north of about 16°N and a cyclonic gyre in the south of about 14°N (Fig. 2f). There exists a relatively strong westward jet in the middle of two gyres, spanning the latitude band from 14°N to 16°N. The previous study shows that the deep SCS circulation can mainly be dominated by the variability of salinity (Wang et al. 2011). One can detect relatively strong salinity anomaly but less temperature anomaly in the deep layer, ranging from 2,000 to 3,500 m (we will come back this issue later). This indicates that TCs can impact salinity structure in the deep layer which in turn influences the deep SCS circulation. The circulation anomaly in the intermediate and deep layer suggests that TCs can impact much deeper ocean.

Figure 3 shows latitude-depth zonal average section of the annual-mean meridional velocity difference between the TCF and NONTCF experiments. The spatial distribution of the velocity difference displays a wave-like pattern. The wave-like signals excited behind traveling TC propagate downward into the ocean interior, and are visible even in the 3,000 m depth. This indicates that the deep ocean circulation anomaly is likely to result from the near inertial oscillation generated by the TC passage propagating downward into the oceanic interior, which can induce abyssal ocean mixing (Zheng et al. 2006; Furuichi et al. 2008; Elipot et al. 2010). Recent observations showed that
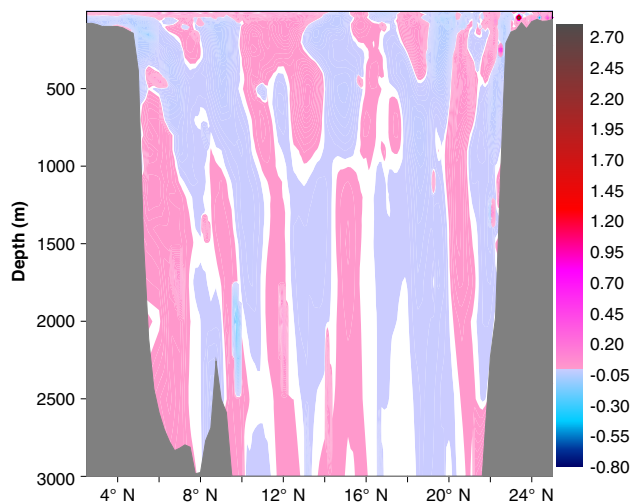
Fig. 3 Latitude-depth zonal average section of the annual-mean meridional velocity difference between the TCF and NONTCF experiments (Unit: cm/s)

Fig. 4 *Left panels* horizontal distribution of annual-mean temperature (Unit: °C) in the NONTCF experiment at **a** the surface and **b** 50 m; *Right panels* the annual-mean temperature difference between the TCF and NONTCF experiments at **c** the surface and **d** 50 m

the TC-induced near inertial waves could reach a depth of 1,200 m in the 10–12 days after TCs passed through (Morozov and Velarde 2008). Using a primitive equation numerical model to investigate propagation of the near initial oscillation induced by winds, Danioux et al. (2008) found that a maximum near inertial vertical velocity exist in 1,700 m depth. Traditionally speaking, the deep SCS circulation is sustained by the deep overflow and internal tide energy flux from Luzon Channel (Tian and Qu 2012). However, our results suggest that the near inertial waves excited by TCs may also be a source of driving the deep SCS circulation. The near inertial energy pathways into small-scale mixing involve complex mechanisms of the energy transfer (Elipot et al. 2010). The present study mainly focuses on the effect of TCs on large-scale circulation and heat transport of the SCS. The detailed effect of the near inertial wave on the deep ocean mixing is beyond the scope of this study.

3.3 Temperature

The TC-induced SST cooling has been known since the 1960s (Leipper 1967). In the SCS, satellite images show that SST can drop largely in response to the passage of typhoons (Lin et al. 2003; Shang et al. 2008). Figure 4 shows annual-mean SST from the NONTCF experiment and the difference between the TCF and NONTCF experiments. The cold anomaly up to −0.16 °C resides in most part of the SCS relative to the NONTCF experiment. There is also positive anomaly up to 0.2 °C along the coastal area of the SCS. The distribution of the SST anomaly can be explained as follows. The upper-ocean response of a TC involves a two-stage process: forced and relaxation stages (Price et al. 1994).
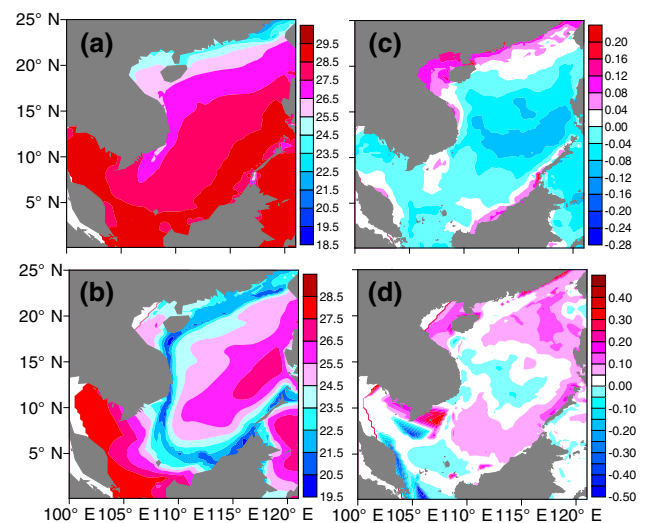
During the forced stage for about half a day, the TC winds drive the mixed layer currents, causing SST cooling by vertical mixing and air-sea heat exchange. The relaxation stage, which is non-local and three-dimensional processes, occurs as part of a primarily baroclinic response associated with upwelling, horizontal advection. The relaxation stage usually has an e-folding time scale of 5–10 days (Price et al. 1994). Due to heat flux from the atmosphere to the ocean, the cold anomaly of SST in the wake of TCs will disappear over an e-folding time of 5–20 days (Price et al. 2008), returning to the normal thermal condition of the Pre-TCs after TCs pass through. Simultaneously, upwelling driven by the positive wind stress curl associated with TCs tends to make surface water divergent, leaving behind a surface cooling at the center of the SCS basin. Due to the half-closed characteristics of the SCS, the warmer surface water accumulates in the coastal areas.

TCs can cause strong and deep mixing in the ocean. Cooling in the mixed layer is usually accompanied by subsurface warming in the greater depths. Generally speaking, the surface heat can be pumped downward to the base of the mixed layer, entering the thermocline (e.g. Emanuel 2001; Sriver and Huber 2007; Sriver et al. 2008). It is shown in Fig. 4b, d that the subsurface warming resides in the most regions of the SCS. The maximum subsurface warming is up to 0.5 °C.

On regional average of the SCS (The region average is taken as 100–121°E, 0–25°N, but the Sulu and Celebes Seas are excluded in this paper), the SST anomaly shows a little cooling, much less than the subsurface warming. SST cooling only reaches about −0.015 °C, while the
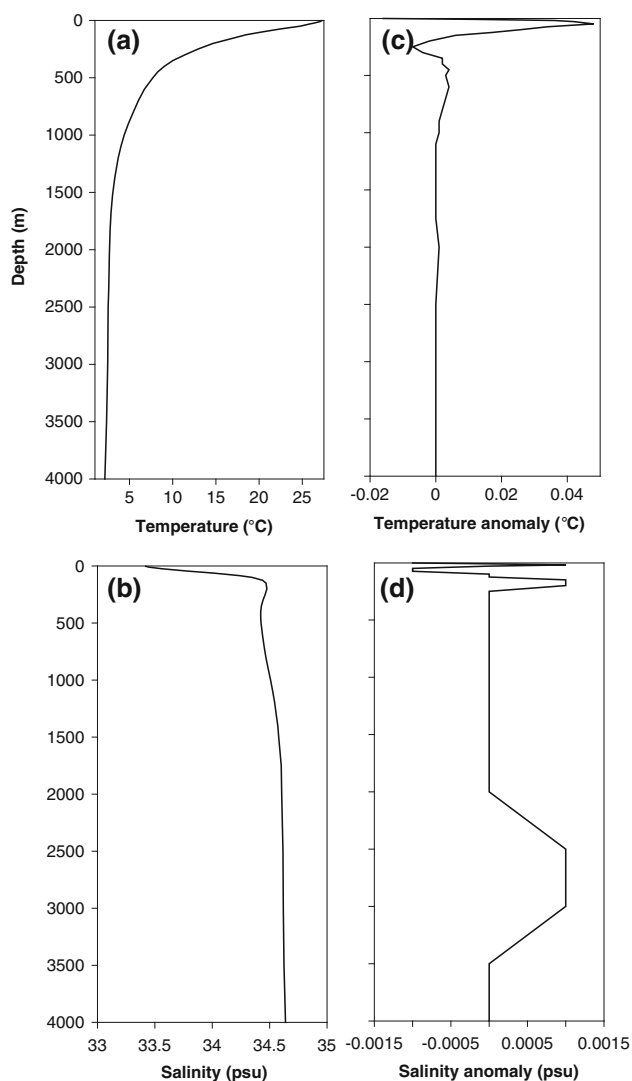
Fig. 5 *Left panels* the SCS regional averages of annual-mean **a** temperature and **b** salinity in the NONTCF experiment; *Right panels* the difference between the TCF and NONTCF experiments for the regional average of **c** temperature and **d** salinity. The regional average is taken as 100–121°E, 0–25°N, but the Sulu and Celebes Seas are excluded

maximum subsurface warming is about 0.045 °C, i.e., three times as many as SST cooling (Fig. 5a, c). This indicates that the surface cooling induced by TCs may mostly be restored to pre-TC background condition by surface radiative flux (Price et al. 2008). It is noted that a footprint of the annual-mean cold anomaly below the thermocline (about −0.01 °C) associated with TC-induced upwelling is visible (Fig. 5c), which is consistent with the results in the South Pacific Ocean (Jullien et al. 2012). This cold anomaly can partly counteract the subsurface warming induced by TCs mixing, which indicates the importance of the TC-induced upwelling in the regional ocean climatology.
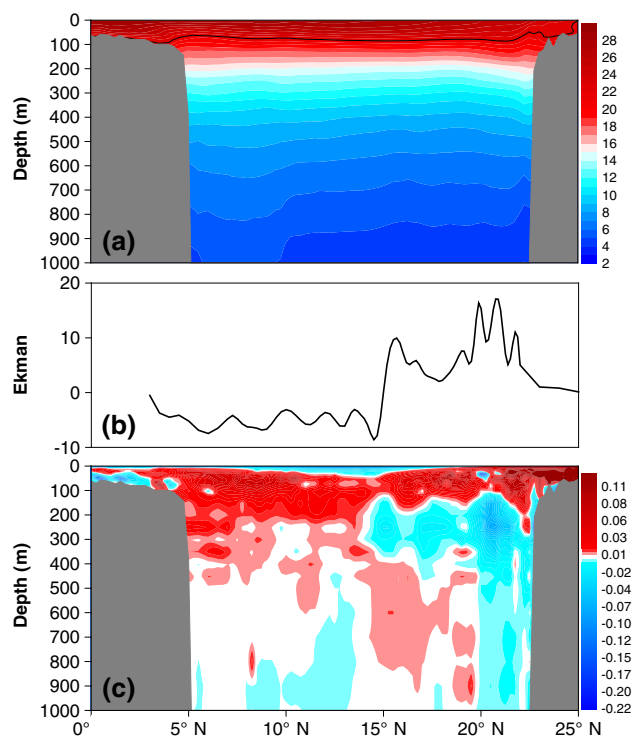
Fig. 6 **a** Latitude-depth zonal average section of the annual-mean temperature for the NONTCF experiment (Unit: °C). **b** Zonal average of the annual-mean Ekman pumping velocity difference between the TCF and NONTCF experiments (Unit: 10^{-6} cm/s) **c** Latitude-depth zonal average section of the annual-mean temperature difference between the TCF and NONTCF experiments (Unit: °C). The *thick line* represents 22 °C isotherm depth in (**a**). The Ekman pumping velocity $w_E = curl(\tau/\rho_w f)$, where τ is wind stress, ρ_w is seawater density, and f is Coriolis frequency. The zonal average region is from 100°E to 121°E, but the Sulu and Celebes Seas are excluded

Figure 6a, c show latitude-depth sections of the NONTCF experiment temperature across the SCS basin from 100–120°E, and the temperature difference between the TCF and NONTCF experiments. The thermocline depth, which can be identified by the 22 °C isotherm, is estimated as 60–80 m (Fig. 6a). A subsurface warming spans the entire SCS, ranging from 0 to 25°N. This maximum warming exists within the thermocline, reaching 0.12 °C in the northern SCS. The 60–80 m depth locates below the base of the mixed layer. At this depth, the warming results largely from TC-induced mixing. Figure 6b shows zonal average of the annual-mean Ekman pumping velocity difference between the TCF and NONTCF experiments. It displays a good correlation between the Ekman pumping and subsurface temperature anomaly. The correlation coefficient is −0.68 at 200 m, which is statistically significant in the 95 % confidence level. In the latitude band of 5–15°N, the significant subsurface warming extends down to about 400 m attributable to the TC-induced downwelling (Fig. 6b, c). In the latitudinal band of
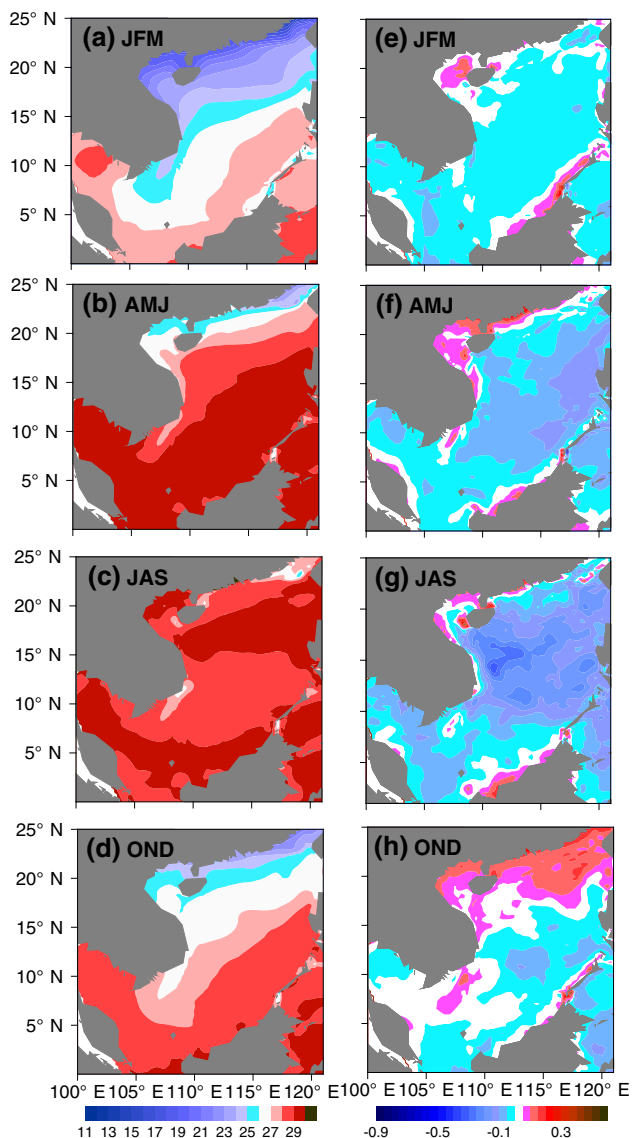
Fig. 7 *Left panels* horizontal distribution of the seasonal average SST (Unit: °C) in the NONTCF experiment during **a** January–March (JFM), **b** April–June (AMJ), **c** July–September (JAS), and **d** October–December (OND); *Right panels* the SST difference (Unit: °C) between the TCF and NONTCF experiments during **e** JFM, **f** AMJ, **g** JAS, and **h** OND

20–22°N, TC-induced upwelling is largely responsible for the maximum cooling below 100 m depth (Fig. 6b, c). These subsurface temperature anomaly patterns are coherent with the upper layer circulation structure induced by TCs (Fig. 2d).

4 Seasonal cycle of ocean thermal response to TCs

The annual-mean response discussed in the last section does not allow us to detect the seasonal effect of TCs. In fact, TCs are mainly active during summer and autumn,
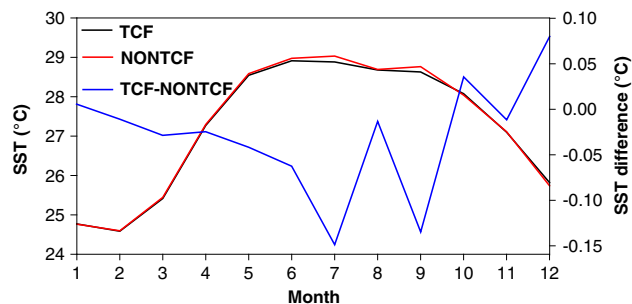

Fig. 8 The SCS monthly average SST, and SST difference between the TCF and NONTCF experiments. The regional average is taken as 100–121°E, 0–25°N, but the Sulu and Celebes Seas are excluded
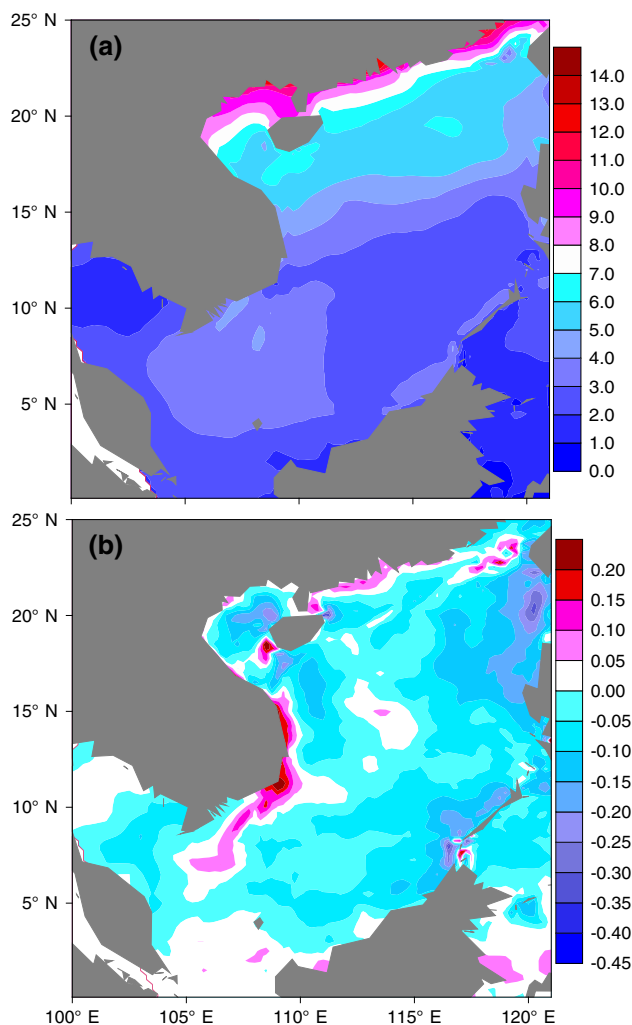

Fig. 9 **a** Seasonal averaged SST amplitude (max minus min SST in 12 months) in the NONTCF experiment and **b** the amplitude difference between the TCF and NONTCF experiments (Unit: °C)

with maximum activity during the period of July–September in the SCS. The horizontal distribution of the seasonal NONTCF SST, the SST difference between the TCF and NONTCF experiments is shown in Fig. 7. During the

spring (AMJ) and summer (JAS) season, the SST anomaly is negative in the nearly entire SCS basin. The most pronouncedly cold anomaly appears in summer, up to −0.5 °C (Fig. 7f, g). The SST anomalies in autumn show a tendency toward positive values in the north of 15°N and about 5°N–10°N. The partly cold anomaly is located at the central sector of the SCS from 10°N to 15°N (Fig. 7h). As a result of intensified wind stress curl and reduced net heat flux from the atmosphere to the ocean, the mixed layer depth in the SCS indeed deepens from October to December and reaches the yearly maximum in December (Qu et al. 2007). Due to the influence of the winter northeast monsoon, there is a deep mixed layer tongue extending southwestward from the Luzon Strait along the continental slope south of China (Qu et al. 2007) where the surface warm anomaly is exceptionally evident (Fig. 7h). This suggests that, during autumn (OND), some of the heat stored under the mixed layer in summer may be taken back to the surface layer. Despite few TCs pass through the SCS in winter (JFM), the weakly negative anomaly still comes forth in most of the SCS basin due to the cumulative effect of TCs on the SCS heat budget (Fig. 7e).

On the regional average of the SCS, SST in the NON-TCF experiment shows a season cycle with the minimum of about 24.5 °C in February and the maximum of about 29 °C in July (Fig. 8). SST in the TCF experiment follows a similar season pattern. However, the TC-induced SST variations are clearly seen in the blue curve. A cold anomaly begins to appear in April, gradually decrease and reach minimum of −0.15 °C until July. During the period from July to November, the cold SST anomaly shows an intraseasonal oscillation, accompanying an increased trend (recovers to normal condition in November).

The seasonal cycle amplitude can be estimated as SST difference between the warmest and coldest months (Fig. 9). It is shown that TCs strongly impact amplitude of the SST seasonal cycle in the pronounced TC regions. TCs play a role of reducing the seasonal cycle in the most regions of the SCS. The reduction is maximum (about −0.45 °C) in the west of the Luzon Strait. The reduction accounts for about 5–20 % decrease of the seasonal cycle amplitude in the most regions of the SCS, which is in better agreement with the estimate of the global basins by Vincent et al. (2012).

Next, we examine vertical distribution of the seasonal temperature anomaly (Fig. 10). In spring, a slight SST cooling in the surface and a warming in the subsurface are apparent in the most of the SCS. The core of the subsurface warming is located at about 35 m depth where the seasonal thermocline exists. A relatively strong cooling embeds below the thermocline with about 160 m depth, extending to about 750 m depth in the latitudinal band of 18°N–21°N, which can be attributed to the TC-induced upwelling.

Similar SST anomaly patterns occur in summer (Fig. 10g). However, the cold and warm anomalies are correspondingly strengthened. For example, the SST cooling is changed from minimum of about −0.02 °C in spring to about −0.2 °C in summer. The core of the subsurface warming is changed from 35 m in spring to about 60 m depth in summer. The cooling underneath the thermocline led by the upwelling in the north of the SCS extends to 1,000 m depth and is intensely increasing up to about −0.5 °C in the cold core. These changes are due to the increase in intensity and frequency of TCs in summer compared with spring. In autumn, the surface cooling in the northern SCS gradually disappears and the subsurface warming extends up to the surface. This is because part of the subsurface warm anomaly stored during summer is fed back to the mixed layer during autumn, which is coincident with the previous analysis (Fig. 7). The cold and warm anomalies in the south of 12°N become quite weak.

An obvious feature in Fig. 10 is that TC-induced temperature anomalies show an alternated pattern of the cold and warm anomalies below the base of the mixed layer in all the seasons, especially in winter. This can be due to that the passage of TCs over the ocean leaves behind the strong inertial oscillations and thus leads to formation of the convergence and divergence zones (Ginis 2002; Rao et al. 2010). This pattern is relatively less evident in summer because the temperature anomalies in summer are dominated by stronger mixing and Ekman pumping induced by TCs.

Figure 11 illustrates the regional average of seasonal temperature variation with depth. In spring, a surface cold anomaly (the minimum of about −0.05 °C) is accompanied by a subsurface warming from 30 to 100 m depth (the maximum of 0.05 °C). The subsurface warming exceeds surface cooling, contributing to an average warming of about 0.01 °C in the upper 600 m. Due to the strengthening of the mixing and upwelling induced by TCs in summer, the mixed layer cooling is increased up to −0.1 °C and the maximum subsurface warming reach 0.05 °C in 60 m depth. An unexpected cold anomaly below the thermocline associated with TC-induced upwelling is observed and partly balances the subsurface warming, which results in a negligibly cold anomaly in the total water column (−0.004 °C) in summer. The warm anomaly resides in the total water column in autumn, which can cause an average warming of 0.03 °C in upper 600 m depth. In winter, the sea surface nearly restores to the normal condition, and the subsurface warming is above the thermocline and shallower than that in summer.

Additionally, Fig. 11 also implies a significant impact on the amount of the heat input associated with TCs. In order to quantify heat input induced by TCs, the ocean heat content anomaly between the TCF and NONTCF
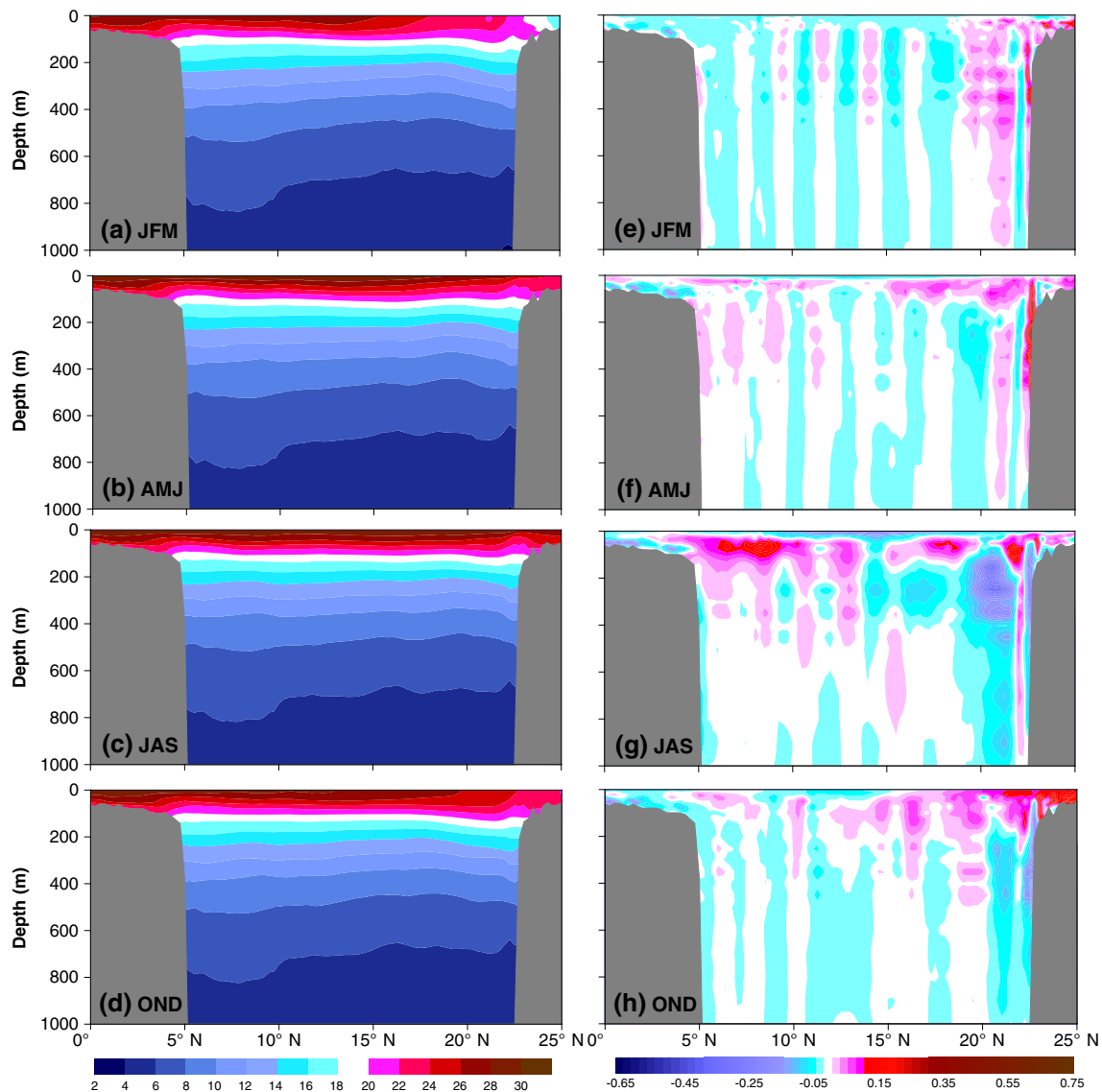
Fig. 10 *Left Panels* latitude-depth zonal average section of the seasonal temperature (Unit: °C) in the NONTCF experiment during **a** JFM, **b** AMJ, **c** JAS, and **d** OND; *Right panels* the seasonal temperature difference (Unit: °C) between the TCF and NONTCF experiments during **e** JFM, **f** AMJ, **g** JAS, and **h** OND. The zonal average is the same as Fig. 6

experiments is calculated for four seasons. The spring heat input is about 0.71×10^{20} J, while there is negligibly small heat loss in summer. The autumn heat input is with the maximum of 1.78×10^{20} J. There is a remaining heat content anomaly with 0.6×10^{20} J in winter. In next section, we will show and discuss the ocean heat transport and heat budget.

5 Influence of TCs on ocean heat transport

Annual average of the total meridional heat transport in the NONTCF experiment and anomalies induced by TCs are displayed in Fig. 12. The total meridional heat transport shows a divergence around 8°N, with an equatorward transport in the south of 8°N and a poleward transport in the north of 8°N (Fig. 12a). The TC-induced poleward and equatorward heat transport anomalies in Fig. 12b indicate a convergence around 6°N in the south of 9°N. In the latitudinal band of 14–25°N, the southward transport in the south of 20°N and the northward transport in the north of 20°N suggest a divergence around 20°N (Fig. 12b). The TC-induced heat transport anomaly is out of phase with the total heat transport in the south of 7.5°N, whereas it is in phase with the total heat transport in the north of 7.5°N. The TC-induced heat transport anomaly accounts for up to 10 % of the total heat transport (Fig. 12c).
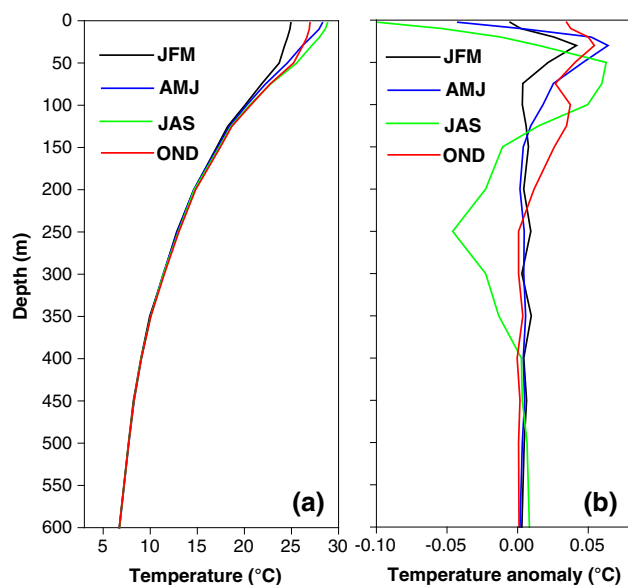
Fig. 11 a The SCS regional average of the seasonal temperature in the NONTCF experiment. **b** The seasonal temperature difference between the TCF and NONTCF experiments. The regional average is the same as Fig. 5

To evaluate influence of TCs on the SCS heat transport, we calculate annual-mean heat budget in the SCS (Table 1). For the calculations of the heat transport through the strait passage, transects are set at the strait passage as shown in Fig. 1b. The heat transport is calculated as follows:

$$OHT = \int_A \rho C_p (T - T_0)\vec{\mathbf{u}} dA, \tag{5}$$

where A represents the transect area from the sea surface to bottom, $\vec{\mathbf{u}}$ is the velocity through transect, ρ is the sea water density, C_p is the specific heat, T is the water temperature, T_0 is a reference temperature. Here, T_0 is simply taken as 0 °C. The heat flux into (out) the SCS is positive (negative).

In the TCF experiment, the SCS contributes to the heat transport of 198TW into the Indonesian maritime continent through Mindoro, Balabac, and Karimata Strait. This value is comparable with the one (200TW, $1TW = 1 \times 10^{12}W$) by Qu et al. (2006a). TCs can significantly increase inflow of the Luzon strait inward the SCS and outflow through the Mindoro Strait to the Sulu Sea. They result in a positive (inward the SCS) heat transport anomaly of 21TW through the Luzon Strait, and a negative (outward the SCS) heat transport anomaly of 37TW through the Mindoro Strait. These heat transport anomalies respectively account for 8 % and 41 % of the total heat transport of the two straits in the TCF experiment. TCs have less influence on the heat
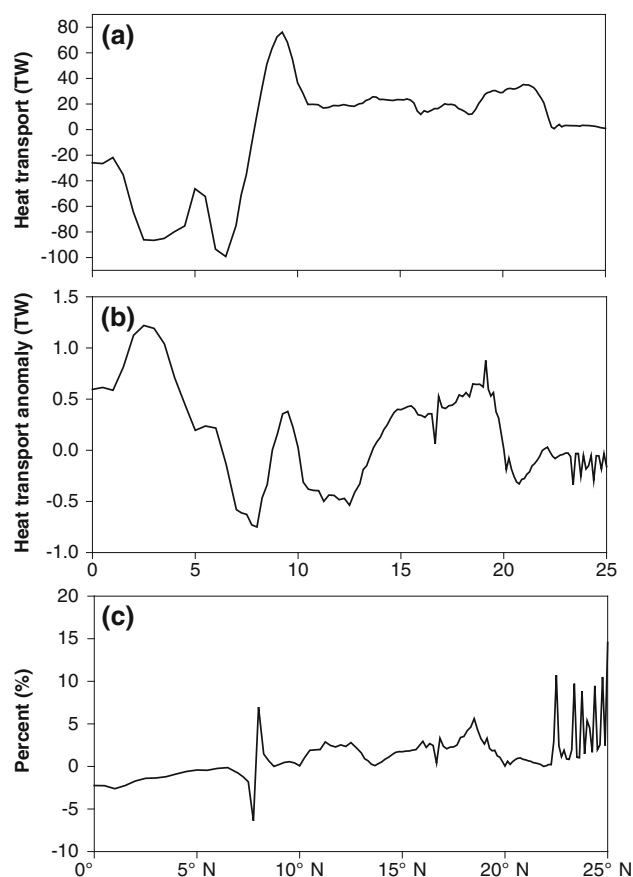

Fig. 12 a The SCS zonal average of the depth-integrated meridional heat transport for the NONTCF experiment. **b** The depth-integrated meridional transport difference between the TCF and NONTCF experiments. **c** The percent of the TC-induced meridional heat transport difference accounting for the total meridional heat transport in the NONTCF experiment. The zonal average region is the same as Fig. 6

Table 1 Annual-mean heat budget for the TCF, NONTCF experiments, and the difference between two experiments over the whole SCS depth (Unit: TW)

	TS	LS	MS	BS	KS	COHU	NOHU
TCF	−124	263	−89	−72	−37	45	10
NONTCF	−125	242	−52	−73	−35	0	0
Difference	1	21	−37	1	−2	45	10

Annual-mean heat transport through the interocean passages of the SCS including Taiwan Strait (TS), Luzon Strait (LS), Mindoro Strait (MS), Balabac Strait (BS), Karimata Strait (KS) is calculated. The cumulative ocean heat uptake (COHU) is calculated as the change rate of the TC seasons heat content anomaly (spring–autumn) between the TCF and NONTCF experiments. Net ocean heat uptake (NOHU) is calculated as the winter heat content anomaly change rate between the TCF and NONTCF experiment. Positive/negative value indicates heat flux inward/outward the SCS

transport through the Taiwan, Balabac and Karimata Straits. The TC-induced heat transport anomalies only account for 0.8, 1, and 3 % of the total heat transport of the

TCF experiment in Taiwan, Balabac and Karimata Straits, respectively. The TC-induced heat transport anomalies through the Mindoro, Balabac and Karimata Straits account for 20 % of the total heat transport through three straits, which can be compensated by the cumulative OHU. The cumulative OHU is defined as a change rate of the TC seasons (spring–autumn) heat content anomaly between the TCF and NONTCF experiments. The cumulative OHU originates from heat pumping by TCs into the ocean interior. The cumulative OHU is estimated as 45TW. The cumulative OHU can be balanced by the following three terms. Based on the winter heat content anomalies between the TCF and NONTCF experiments, we estimate about 22 % (10TW) of the cumulative OHU left within the winter thermocline, i.e. net OHU. About 35 % (16TW) of the cumulative OHU is advected outward the SCS through Mindoro Strait. The remaining 43 % (19TW) of the cumulative OHU is returned to the mixed layer and released back to the atmosphere as a result of seasonal mixed layer deepening.

6 Summary and discussion

In this study, we use an ocean GCM to investigate effects of TCs on the SCS large-scale circulation and heat transport. The ocean GCM at a 1/8° resolution in the SCS employs a data assimilation system to assimilate observational data including in situ temperature and salinity profiles, altimetry and satellite SST, which allows representing better the SCS circulation structure from mesoscale to large scale without the passage of TCs. Performing the sensitive experiments, we focus on the role of TC-induced mixing and dynamical process in the SCS large-scale circulation and heat transport.

The ocean GCM results reveal that the large-scale circulation structure in the upper layer can be mainly impacted by the positive wind stress curl input by TCs, which is consistent with Wang et al. (2009). However, an unexpected effect on the deep SCS circulation is found. The circulation anomaly in the deep layer suggests that effects of TCs can penetrate much deeper ocean. This deep effect is likely to result from the near inertial oscillation generated by TCs. The inertial oscillation can propagate downward to the oceanic interior, which induces abyssal mixing (Zheng et al. 2006; Furuichi et al. 2008; Elipot et al. 2010). The interaction between the inertial oscillations generated by TC and a mesoscale eddy field was recently studied by Zhai et al. (2005). It is shown that the propagation of near-inertial energy is strongly enhanced by the presence of anticyclonic eddies acting as a conduit to the deep ocean. Using a numerical model to investigate propagation of the near initial oscillation in the mesoscale eddy

fields, Danioux et al. (2008) found that a maximum near inertial vertical velocity exist in 1,700 m depth. This is attributed to refraction by the eddy relative vorticity triggering propagation of the near inertial oscillation. This reveals a pathway by which wind energy may have a significant impact on small-scale mixing in the deep ocean. In the SCS, whenever the wind forcing contains energy at the inertial frequencies, in regions of high eddy activity the transfer of wind energy from the atmosphere into the ocean is enhanced below the mixed-layer by the near inertial oscillations (Cardona and Bracco 2012). There are many mesoscale eddies embedded in the large SCS gyres, which was observed from both hydrographic (e.g., Chu et al. 1998) and altimeter data (e.g., Wang et al. 2003). Thus, it is suggested that the interaction between the near initial oscillation induced by TCs and ocean mesoscale eddy is important for understanding how near-inertial energy enters the deep oceanic interior and finally affects deep SCS circulation. However, the near-inertial energy pathways transforming into small-scale mixing involve complex mechanisms of the energy transfer. This deserves a further investigation in future studies.

The influence of TCs on the ocean has a significant seasonal cycle due to seasonal characteristic of the TCs occurrence. The TC-induced surface cooling in summer result in a 5–20 % reduction of the SST seasonal cycle in most regions of the SCS, which basically agrees with global scale findings (Vincent et al. 2012). The present study also shows that TCs can result in a summer intraseasonal oscillation of the SST anomaly with the amplitude of about 0.15 °C. The Indian and East Asian monsoon systems can affect the SCS (e.g., Lau et al. 1998). Intraseasonal oscillation is an important part of the SCS summer monsoon variability. It significantly affects the local weather and climate as well as global atmospheric circulation (Mao and Chan 2005; Wu 2010). Roxy and Tanimoto (2012) found that the intraseasonal SST anomaly in summer is significantly correlated with the precipitation anomaly in the SCS. The summer intraseasonal SST anomalies tend to form a favorable condition for convective activity and sustain enhanced precipitation during the SCS summer monsoon. Thus, it is likely to provide a hint that the intraseasonal oscillation of the TC-induced SST anomaly can be connected with the intraseasonal variability of SCS summer monsoon and finally influences the climate system in the SCS and adjacent regions.

The ocean GCM results show that the TC-induced subsurface warming mostly occurs in the seasonal thermocline with a significant season variation. There is a cumulative OHU of 45TW in the total TC season. The cumulative OHU can be balanced by three terms. Firstly, about 22 % of the cumulative OHU is left within the winter thermocline. Secondly, about 35 % of the cumulative OHU

is mostly advected outward the SCS through Mindoro Strait. Finally, about 43 % of the heat is returned to the mixed layer and released back to the atmosphere, as a result of seasonal mixed layer deepening.

The analyses confirm that TCs have two effects on the heat transport of the SCS. Firstly, the wind stress curls related to TCs impact the structure of SCS circulation, then heat transport. Secondly, TCs pump the surface heat downward to the thermocline, increasing the heat injection from the atmosphere to the ocean. These two effects together amplify the surface heat of the SCS southward away the SCS through Mindoro and Karimata Straits. The TC-induced heat transport anomalies from the Mindoro, Balabac and Karimata Straits account for 20 % of the total heat transport. Performing the sensitive experiment in numerical ocean model, Tozuka et al. (2007) suggested that the SCSTF significantly (by as much as 47 %) reduces the ITF heat transport. It potentially regulates SST pattern in the tropical Indian and Pacific Oceans. Due to the significant effect of TC-induced ocean heat transport anomaly on SCSTF, an implication of this study is that ocean models need to simulate this TC effect on heat transport in order to correctly evaluate the role of the SCSTF in regulating upper ocean circulation and climate in the Indonesian maritime continent and its adjacent regions.

The CCMP winds used in this study can usually better depict the TC locations and capture the cyclonic circulation patterns. However, the winds can't most represent the observed TC maximum sustained wind speed. Due to the underestimation of wind speed, we might underestimate the mixing and heat pumping effects of TCs. In the present study, we only focus on the effects of momentum flux by TCs on the ocean heat transport. However, other processes associated with TCs may also be important. For example, recent modeling and observational studies show potential effects of TC rainfall on thermohaline circulation (Hu and Meehl 2009) and local ocean heat budget (Wang et al. 2012; Jourdain et al. 2013). Thus, coupled ocean–atmosphere models are needed to study the role of TCs in the SCS climate system.

References

Cardona Y, Bracco A (2012) Enhanced vertical mixing within mesoscale eddies due to high frequency winds in the South China Sea. Ocean Model 42:1–15

Chu PC, Lu S, Chen Y (1997) Temporal and spatial variabilities of the South China Sea surface temperature anomaly. J Geophys Res 102:20937–20955

Chu PC, Fan CW, Lozano CJ, Kerling JL (1998) An airborne expendable bathythermograph survey of the South China Sea, May 1995. J Geophys Res 103:21637–21652

Danioux E, Klein P, Priviere P (2008) Propagation of wind energy into the deep ocean through a fully turbulent mesoscale eddy field. J Phys Oceanogr 38:2224–2241. doi:10.1175/2008JPO3821.1

Dare RA, Mcbride JL (2011) Sea surface temperature response to tropical cyclones. Mon Weather Rev 139:3798–3808. doi:10.1175/MWR-D-10-05019.1

Ducet N, Le Traon P-Y, Reverdin G (2000) Global high resolution mapping of ocean circulation from TOPEX/Poseidon and ERS-1 and -2. J Geophys Res 105:19477–19498

Elipot S, Lumpkin R, Prieto G (2010) Modifications of inertial oscillations by the mesoscale eddy field. J Geophys Res. doi:10.1029/2009JC05679

Emanuel KA (2001) Contribution of tropical cyclones to meridional heat transport by the oceans. J Geophys Res 106:14771–14781

Emanuel KA (2005) Increasing destructiveness of tropical cyclones over the past 30 years. Nature 436:686–688

Fairall CW, Bradley EF, Hare JE, Grachev AA, Edson JB (2003) Bulk parameterization on air–sea fluxes: Updates and verification for the COARE algorithm. J Clim 16:571–591

Fedorov AV, Brierley CM, Emanuel KA (2010) Tropical cyclones and permanent El Niño in the early Pliocene epoch. Nature 463:1066–1070

Furuichi N, Hibiya T, Niwa Y (2008) Model-predicted distribution of wind-induced internal wave energy in the world's oceans. J Geophys Res 113(C9):2156–2202

Ginis I (2002) Tropical cyclone-ocean interactions, chapter 3, in atmosphere-ocean interactions. In: Perrie W (ed) WIT Press Advances in fluid mechanics series 33: 83–114

Gordon AL (2005) Oceanography of Indonesian seas and their throughflow. Oceanography 18:14–27

Gordon AL, Susanto RD, Vranes K (2003) Cool Indonesian throughflow as a consequence of restricted surface layer flow. Nature 425:824–828

Han GJ, Li W, Zhang XF, Li D, He ZJ, Wang XD, Wu XR, Yu T, Ma JR (2011) A regional ocean reanalysis system for coastal waters of China and adjacent seas. Adv Atmos Sci 28(3):682–690

Hart RE, Maue RN, Watson MC (2007) Estimating local memory of tropical cyclones through MPI anomaly evolution. Mon Weather Rev 135:3990–4005

Hu A, Meehl GA (2009) Effect of the Atlantic hurricanes on the oceanic meridional overturning circulation and heat transport. Geophys Res Lett. doi:10.1029/2008GL036680

Jansen MF, Ferrari R (2009) Impact of the latitudinal distribution of tropical cyclones on ocean heat transport. Geophys Res Lett. doi:10.1029/2008GL036796

Jansen MF, Ferrari R, Mooring TA (2010) Seasonal versus permanent thermocline warming by tropical cyclones. Geophys Res Lett. doi:10.1029/2009GL041808

Jourdain NC, Lengaigne M, Vialard J, Madec G, Menkes CE, Vincent EM, Samson G, Jullien S, Barnier B (2013) Observation-based estimates of ocean mixing inhibition by heavy rainfall under tropical cyclones. J Phys Oceanogr 43:205–221

Jullien S, Menkes CE, Marchesiello P, Jourdain NC, Lengaigne M, Koch-Larrouy A, Lefèvre J, Vincent EM, Faure V (2012) Impact of tropical cyclones on the heat budget of the South Pacific Ocean. J Phys Oceanogr 42:1882–1905

Korty RL, Emanuel KA, Scott JR (2008) Tropical cyclone induced mixing and climate: application to equable climates. J Clim 21:638–654

Kossin JP, Knapp KR, Vimont DJ, Murnane RJ, Harper BA (2007) A globally consistent reanalysis of hurricane variability and trends. Geophys Res Lett. doi:10.1029/2006GL028836

Large WG, Pond S (1981) Open ocean momentum flux measurements in moderate to strong winds. J Phys Oceanogr 11:324–336

Lau KM, Wu HT, Yang S (1998) Hydrologic processes associated with the firs transition of the Asian summer monsoon: a pilot satellite study. Bull Am Meteorol Soc 79(9):1871–1882

Leipper DF (1967) Observed ocean conditions and Hurricane Hilda, 1964. J Atmos Sci 24:182–196

Li L, Qu T (2006) Thermohaline circulation in the deep South China Sea basin inferred from oxygen distributions. J Geophys Res. doi:10.1029/2005JC003164

Li W, Xie YF, He ZJ, Liu KX, Han GJ, Ma JR, Li D (2008) Application of the multi-grid data assimilation scheme to the China Seas' temperature forecast. J Atmos Oceanic Technol 25(11):2106–2116

Li W, Xie YF, Deng SM, Wang Q (2010) Application of the multigrid method to the two-dimensional doppler radar radial velocity data assimilation. J Atmos Oceanic Technol 27(2):319–332

Lin I-I, Liu WT, Wu C-C, Wong GTF, Hu C, Chen Z, Liang W-D, Yang Y, Liu K-K (2003) New evidence for enhanced primary production triggered by tropical cyclone. J Geophys Res. doi:10.1029/2003GL017141

Liu LL, Wang W, Huang RX (2008) The mechanical energy input to the ocean induced by tropical cyclones. J Phys Oceanogr 38:1253–1266

Mao JY, Chan JCL (2005) Intraseasonal variability of the South China Sea summer monsoon. J Clim 18(13):2388–2402

Mellor GL, Hakkinen S, Ezer T, Patchen R (2002) A generalization of a sigma coordinate ocean model and an intercomparison of model vertical grids. In: Pinard N, Woods J (eds) Ocean forecasting: conceptual basis and applications. Springer, Berlin, pp 55–72

Morozov EG, Velarde MG (2008) Inertial oscillations as deep ocean response to hurricanes. J Oceanogr 64(4):495–509. doi:10.1007/s10872-008-0042-0

Oey LY, Ezer T, Wang DP, Yin XQ, Fan SJ (2006) Loop current warming by Hurricane Wilma. Geophys Res Lett. doi:10.1029/2006GL02587

Pasquero C, Emanuel K (2008) Tropical cyclones and transient upper-ocean warming. J Clim 21:149–162

Powell MD, Vichery PJ, Reinhold T (2003) Reduced drag coefficient for high wind speeds in tropical cyclones. Nature 422:279–283. doi:10.1038/nature01481

Price JF, Sanford TB, Forristall GZ (1994) Forced stage response to a moving hurricane. J Phys Oceanogr 24:233–260

Price JF, Morzel J, Niiler PP (2008) Warming of SST in the cool wake of a moving hurricane. J Geophys Res. doi:10.1029/2007JC004393

Qu T (2000) Upper-layer circulation in the South China Sea. J Phys Oceanogr 30:1450–1460

Qu T (2001) Role of ocean dynamics in determining the mean seasonal cycle of the South China Sea surface temperature. J Geophys Res 106:6943–6955

Qu T, Du Y, Meyers G, Ishida A, Wang D (2005) Connecting the tropical Pacific with Indian Ocean through South China Sea. Geophys Res Lett. doi:10.1029/2005GL024698

Qu T, Du Y, Sasaki H (2006a) South China sea throughflow: a heat and freshwater conveyor. Geophys Res Lett. doi:10.1029/2006GL028350

Qu T, Girton JB, Whitehead JA (2006b) Deepwater overflow through Luzon Strait. J Geophys Res. doi:10.1029/2005JC003139

Qu T, Du Y, Gan J, Wang D (2007) Mean seasonal cycle of isothermal depth in the South China Sea. J Geophys Res. doi:10.1029/2006JC003583

Rao AD, Madhu J, Jain I, Ravichandran M (2010) Response of subsurface waters in the eastern Arabian Sea to tropical cyclones. Estuar Coast Shelf Sci 89:267–276

Reynolds RW, Smith TM, Liu C, Chelton DB, Casey KS, Schlax MG (2007) Daily high-resolution blended analyses for sea surface temperature. J Clim 20:5473–5496

Roxy M, Tanimoto Y (2012) Influence of sea surface temperature on the intraseasonal variability of the South China Sea summer monsoon. Clim Dyn 39(5):1209–1218. doi:10.1007/s00382-011-1118-x

Scoccimarro E, Gualdi S, Bellucci A, Sanna A, Fogli PG, Manzini E, Vichi M, Oddo P, Navarra A (2011) Effects of tropical cyclones on ocean heat transport in a high resolution coupled general circulation model. J Clim 24(16):4368–4384. doi:10.1175/2011JCLI4104.1

Shang S-L, Li L, Sun F, Wu J, Hu C, Chen D, Ning X, Qiu Y, Zhang C, Shang S (2008) Changes of temperature and bio-optical properties in the South China Sea in response to typhoon Lingling, 2001. Geophys Res Lett. doi:10.1029/2008GL033502

Sriver RL, Huber M (2007) Observational evidence for an ocean heat pump induced by tropical cyclones. Nature 447:577–580. doi:10.1038/nature05785

Sriver RL, Huber M, Nusbaumer J (2008) Investigating tropical cyclone-climate feedbacks using the TRMM Microwave Imager and the Quick Scatterometer. Geochem Geophys Geosyst. doi:10.1029/2007GC001842

Sriver RL, Goes M, Mann ME, Keller K (2010) Climate response to tropical cyclone-induced ocean mixing in an Earth system model of intermediate complexity. J Geophys Res. doi:10.1029/2010JC006106

Tian J, Qu T (2012) Advances in research on the deep South China Sea circulation. Chin Sci Bull 57(24):3115–3120

Tozuka T, Qu T, Yamagata T (2007) Effect of South China Sea through flow on the Makassar strait throughflow. Geophys Res Lett. doi:10.1029/2007GL030420

Troccoli A, Balmaseda MA, Segschneider J, Vialard J, Anderson DLT, Haines K, Stockdale T, Vitart F, Fox AD (2002) Salinity adjustments in the presence of temperature data assimilation. Mon Weather Rev 130:89–102

Vincent EM, Madec G, Lengaigne M, Koch-Larrouy A, Vialard J (2012) Influence of tropical cyclones on sea surface temperature seasonal cycle and ocean heat transport. Clim Dyn. doi:10.1007/s00382-012-1556-0

Wang W, Wang C (2006) Formation and decay of the spring warm pool in the South China Sea. Geophys Res Lett. doi:10.1029/2005GL025097

Wang G, Su J, Chu PC (2003) Mesoscale eddies in the South China Sea observed with altimeter data. Geophys Res Lett. doi:10.1029/2003GL018532

Wang C, Wang W, Wang D, Wang Q (2006a) Interannual variability of the South China Sea associated with El Niño. J Geophys Res. doi:10.1029/2005JC003333

Wang D, Liu Q, Huang R, Du Y, Qu T (2006b) Interannual variability of the South China Sea throughflow inferred from wind data and an ocean data assimilation product. Geophys Res Lett. doi:10.1029/2006GL026316

Wang G, Su J, Ding Y, Chen D (2007) Tropical cyclones genesis over the South China Sea. J Mar Syst 68(3–4):318–326

Wang G, Ling Z, Wang C (2009) Influence of tropical cyclones on seasonal ocean circulation in the South China Sea. J Geophys Res. doi:10.1029/2009JC005302

Wang G, Xie S-P, Qu T, Huang R-X (2011) Deep South China Sea circulation. Geophys Res Lett. doi:10.1029/2010GL046626

Wang J-W, Han W, Sriver RL (2012) Impact of tropical cyclones on the ocean heat budget in the Bay of Bengal during 1999. Model configuration and evaluation. J Geophys Res, Part I. doi:10.1029/2012JC008372

Wu R (2010) Subseasonal variability during the South China Sea summer monsoon onset. Clim Dyn 34(5):629–642. doi:10.1007/s00382-009-0679-4

Wu C-R, Shaw P-T, Chao S-Y (1998) Seasonal and interannual variations in the velocity field of the South China Sea. J Oceanogr 54:361–372

Wyrtki K (1961) Physical oceanography of the southeast Asian waters. Naga Rep 2 Scripps Inst. of Oceanogr. La Jolla, Calif, pp 195

Zhai X, Greatbach R, Zhao J (2005) Enhanced vertical propagation of storm-induced near-inertial energy in an eddying ocean channel model. Geophys Res Lett. doi:10.1029/2005GL023643

Zheng Q, Lai RJ, Huang NE, Pan J, Liu WT (2006) Observation of ocean current response to 1998 Hurricane Georges at Gulf of Mexico. Acta Oceanologica Sinica 25:1–14

Zhu J, Yan CX (2006) Nonlinear balance constraints in 3DVAR data assimilation. Sci China 49:331–336